1   Pre-print Statement for

2   # "Fe₅S₂ identified as a host for sulfur in Earth's core"

3   **Claire C. Zurkowski[a][†], Barbara Lavina[b,c], Abigail Case[a], Kellie Swadba[a], Stella Chariton[b],**
4   **Vitali B. Prakapenka[b], Andrew J. Campbell[a]**

5

6   [a]The University of Chicago, Department of the Geophysical Sciences, 5734 S Ellis Ave, Chicago, IL 60637, USA
7   [b]Center for Advanced Radiation Sources, The University of Chicago, 9700 South Cass Avenue, Lemont, IL 60439,
8   USA
9   [c]X-ray Science Division, Advanced Photon Source, Argonne National Laboratory, Lemont, IL 60439, USA
10   [†]Now at Earth and Planets Laboratory, Carnegie Institution for Science, 5251 Broad Branch Road, NW,
11   Washington, DC 20015, USA

12

13

14   Corresponding Author: Claire Zurkowski, czurkowski@carnegiescience.edu

15

23

24

25

26

27

28

29

30

31

32

Fe₅S₂ identified as a host of sulfur in Earth and planetary cores

Claire C. Zurkowski[a][†], **Barbara Lavina**[b,c], **Abigail Case**[a], **Kellie Swadba**[a], **Stella Chariton**[b], **Vitali Prakapenka**[b], **Andrew J. Campbell**[a]

[a]University of Chicago, Department of the Geophysical Sciences, 5734 S Ellis Ave, Chicago, IL 60637, USA
[b]Center for Advanced Radiation Sources, 9700 South Cass Avenue, Building 434A, Argonne, IL 60439, USA
[c]X-ray Science Division, Advanced Photon Source, Argonne National Laboratory, Argonne, IL 60439, USA
[†]Now at Earth and Planets Laboratory, Carnegie Institution for Science, 5251 Broad Branch Road, NW, Washington, DC 20015, USA

Corresponding Author: Claire Zurkowski, czurkowski@carnegiescience.edu

ABSTRACT

Cosmochemical considerations suggest that sulfur is a light alloying element in rocky planetary cores of varying sizes and oxidation states. High pressure-temperature (P-T) iron-sulfide phase relations therefore play a role in inner core crystallization and outer core thermochemical convection in a wide range of planetary bodies. The iron-saturated Fe-S phase relations were investigated to 200 GPa and 3250 K using single-crystal and powder X-ray diffraction techniques in a laser-heated diamond anvil cell. At high temperatures between 120 and 200 GPa, a hexagonal sulfide was synthesized with recrystallized hcp-Fe. The unit-cell parameters and diffraction intensities reveal an Fe_5S_2 stoichiometry adopting the Ni_5As_2 structure ($P6_3cm$, $Z = 6$). Fe_5S_2 is characterized by significant Fe-Fe bonding, complex coordination environments, and positional disorder and polytypism along the c-axis. Upon heating at 120 GPa, I-4 Fe_3S is observed to break down into Fe_5S_2 + Fe, whereas with heating above 120 GPa, Fe_2S + Fe reacts to form Fe_5S_2 + Fe at high temperatures. A $C23$–$C37$ Fe_2S transition is observed above 130 GPa. These results establish that Fe_5S_2 is the stable Fe-rich sulfide across much of Earth's outer core and will crystallize over an extensive depth up to the core-mantle boundary as the core

62 cools overtime. The increased metal-metal bonding observed in Fe_5S_2 compared to the other high

63 *P-T* iron sulfides would likely contribute to signatures of higher conductivity from regions of

64 Fe_5S_2 crystallization. As Earth's core is multicomponent, Fe_5S_2 could further serve as a host for

65 Ni and Si as has been observed in the related meteoritic phase perryite, $(Fe, Ni)_8(P, Si)_3$, adding

66 intricacies to elemental partitioning during inner core crystallization. The stability of Fe_5S_2

67 presented here is key to understanding the role of sulfur in the crystallization sequences that

68 drive the geodynamics and dictate the structures of Earth and rocky planetary cores.

69

1. INTRODUCTION

71   Earth and the terrestrial planets are composed of silicate mantles and iron-rich metallic

72 cores (e.g. Birch 1952; Mcdonough and Sun 1995). Earth's core is comprised of a convecting

73 liquid metal outer core and an actively crystallizing, denser inner core (Birch 1952; Dziewonski

74 and Anderson 1981; Fearn and Loper, 1981). The seismically determined 3-8% density deficit in

75 Earth's core compared to pure iron is thought to be accounted for by cosmochemically abundant

76 light alloying elements, such as Si, O, S, C, and H (Masters and Gubbins, 2003; Irving et al.

77 2018; Kuwayami et al. 2020; McDonough 2003), that introduce complex *P-T*-dependent melting

78 and crystallization thermodynamics and help drive core convection as planets cool over time

79 (Fearn and Loper, 1981; Stevenson 1981; 1988; Nimmo 2015).

80   While there remains no method to directly sample Earth's or any terrestrial planetary

81 core, iron meteorites are recognized as core relics of disrupted planetesimals, and have long

82 provided insight into the light elements that sequester into the metallic component of planetary

83 interiors (e.g. Scott and Wasson 1975; Malvin et al. 1984). Of the candidate core-alloying

84 elements, sulfur is present in nearly all iron meteorites, suggesting that sulfur is a core alloying

85 element in rocky planets of varying sizes, oxidation states, and formation histories (Scott and

86 Wasson 1975; Jones and Drake, 1983; Kruijer et al. 2014). Sulfur easily alloys with iron to high

87 pressures and temperatures, it is depleted in the silicate mantle compared to chondrites, and it

88 lowers the melting temperature of pure iron (e.g. Evans 1970; Fei 1995; McDonough and Sun

89 1995; Fei et al. 1997; Ozawa et al. 2013; Tateno et al. 2019). It follows that during the high

90 energy impact conditions of late stage proto-Earth formation, sulfur would have facilitated metal

91 melt formation and density driven core segregation (Ringwood 1966; Murthy and Hall 1970;

92 Shannon and Agee, 1996; Stevenson, 1988; Yoshino et al., 2003). Examination of the structural

93 properties of iron sulfides at high P-T is therefore fundamental to characterizing the chemistry

94 and thermodynamics of Earth and planetary cores.

95   The Fe-S phase relations are sensitive to P-T-composition conditions, and numerous Fe-

96 rich sulfide compounds have been observed: FeS, Fe_3S_2, Fe_2S, and Fe_3S (Evans 1970; King and

97 Prewitt 1982; Fei et al. 1995; Fei et al. 1997; Fei et al. 2000; Koch-Müller et al. 2002; Kamada et

98 al. 2010; Ozawa et al. 2013; Mori et al. 2017; Tateno et al. 2019). Fe_3S is reported to be the

99 stable Fe-rich sulfide between 21 and 250 GPa (Fei et al. 2000; Kamada et al. 2010; Ozawa et al.

100 2013), making it relevant at Earth's outer core conditions. Single crystal analysis of recovered

101 Fe_3S from 21 GPa establishes that it adopts a Fe_3P-type structure (I-4, Z=8) (Fei et al. 2000), and

102 no structural transitions have been reported in Fe_3S to 250 GPa (Ozawa et al. 2013; Kamada et

103 al. 2010; Thompson et al. 2020; Seagle et al. 2006; Morard et al. 2008; Mori et al. 2017). Above

104 ~250 GPa, Fe_3S breaks down at low temperatures into a B2 FeS + Fe phase assemblage, and

105 FeS+Fe reacts at high temperatures to form C37 Fe_2S + Fe at 306 GPa (Ozawa et al. 2013; Mori

106 et al. 2017; Tateno et al. 2019).

107   Although tetragonal Fe_3S has been reported to be stable to pressures encompassing

108   Earth's upper-to-mid-outer core, crystal structure analysis of Fe_3S has not been conducted at

109   Earth's core pressures, and unit-cell parameters for Fe_3S have only been reported up to 120 GPa

110   at high temperatures (Seagle et al. 2006; Morard et al. 2008; Thompson et al. 2020). In the

111   current study, Fe-rich Fe-S compositions were probed using single crystal and powder X-ray

112   diffraction techniques which revealed that at high-temperatures between 120–200 GPa, hcp-Fe

113   coexists with a hexagonal Fe_5S_2 sulfide (Ni_5As_2-type, $P6_3cm$, $Z = 6$). This complex crystal

114   structure exhibits pervasive positional disorder and various stacking variations, such that single-

115   crystal diffraction techniques were critical in identifying its crystal-chemistry. Increasing across

116   the pressure range of 120–200 GPa, we find that Fe_3P-type Fe_3S + Fe, $C23$ Fe_2S + Fe , and $C37$

117   Fe_2S + Fe all react at high temperatures to form Fe_5S_2 + hcp-Fe. The single-crystal derived

118   structures for $C23$ Fe_2S, I-4 Fe_3S, and $C37$ Fe_2S are also presented. The stability of Fe_5S_2 with

119   recrystallized iron to 200 GPa at high temperatures reveals that Fe_5S_2 will eventually crystallize

120   over a significant depth range of Earth's outer core.

121

2. MATERIALS AND METHODS

122

123   Experiments targeting multigrain synthesis in the Fe-S system consisted of mixtures of Fe

124   (99.9+%, <10μm, Alfa Aesar) and iron sulfide (FeS, 99.99%, Alfa Aesar) in Fe+12.5 wt% S

125   ($Fe_{80}S_{20}$), Fe + 23 wt% S ($Fe_{67}S_{33}$) compositions. The Fe-FeS compositions were ground in

126   ethanol in a pestle and mortar for 1 hour then mixed dry for a short interval to homogenize any

127   density settling during alcohol evaporation.

128   Pressure was generated using BX-90-type (Kantor et al. 2012) diamond anvil cells (DAC)

129   with type 1 Boehler-Almax conical diamonds and seats, and Mao symmetric-type DACs with

130 Type 1 standard cut diamonds mounted on tungsten carbide of cubic-boron nitride (cBN) seats.

131 Diamond culets ranged from 150-50 μm in diameter. Foils of $Fe_{80}S_{20}$ or $Fe_{67}S_{33}$ were produced

132 by pressing the Fe–S starting powders between two ungasketed diamond anvils, then loaded

133 between pellets of KCl or SiO_2. Sample chambers ranged from 180-25 μm in diameter and were

134 drilled from pre-indented rhenium gaskets. Samples were dried at 100º C for 30 minutes prior to

135 pressurization.

136   Angle dispersive X-ray diffraction (XRD) experiments were conducted at Argonne

137 National Laboratory, Sector 13 ID-D, of the Advanced Photon Source. At Sector 13 ID-D, a 2.5

138 μm x 3.54 μm full width, half maximum (FWHM) monochromatic X-ray beam tuned to 37 or 42

139 keV was utilized, and diffracted X-rays were collected with a CdTe 1M Pilatus detector. Sample-

140 to-detector geometries were calibrated using a LaB_6 NIST standard and a single crystal of

141 enstatite was used for calibration of the rotational geometry of the X-ray beam and detector.

142   Double-sided laser heating and *in-situ* XRD collection took place at Sector 13 ID-D. Fiber

143 lasers shaped with ~10 μm radius flat tops were aligned with the X-ray beam using the X-ray

144 fluorescence of the sample pressure media or the gasket (Prakapenka et al., 2008). During

145 heating, thermal emission from a 6 μm central region of the laser-heated spot was measured

146 spectroradiometrically and fit to a gray body approximation (Heinz and Jeanloz, 1987). A 3%

147 temperature correction was then applied to correct for axial gradients through the sample

148 (Campbell et al., 2007; 2009). The laser power on each side of the sample was adjusted to

149 maintain uniform double-sided heating and X-ray diffraction and temperature measurements

150 were collected every ~200 K with 1s exposure times. Samples were typically quenched at high

151 temperatures within 30-45 minutes of heating or after a phase transition and suitable grain

152 growth was observed. Powder diffraction patterns were processed using Dioptas (Prescher and

153   Prakapenka, 2015) and CrysalisPro (Rigaku OD, 2018). Pressure was determined using the

154   equation of state of hcp-Fe (Dewaele et al. 2006).

155   Upon quenching, X-ray diffraction maps of the heated spot were collected across a 100

156   μm^2 square region in 3 μm steps. Map locations showing high intensity, spotty diffraction

157   patterns were chosen for multigrain single-crystal type X-ray diffraction collection approach, as

158   these features indicate high-temperature induced crystallite growth. At chosen map locations, X-

159   ray diffraction images were collected across ±17 to ±30° rotational scans in 0.25°–0.5° steps with

160   1– 4 s exposure times. The diffraction reflections were then mapped in the reciprocal space and

161   target grains were identified and separated from reflections associated with the pressure media,

162   iron, and diamond (Rigaku OD, 2018).

163   Target Fe-S lattices were then indexed, and the peak intensities were integrated and

164   reduced using CrysalisPro (Rigaku OD, 2018). Absorption corrections and scaling factors were

165   applied to the structure factors in CrysalisPro using the multi-scan method via the Scale3

166   Abspack program (Rigaku OD, 2018). The final structure factors and lattice geometries were

167   then refined to known structure models (El-Boragy et al. 1970; Oryshchyn et al. 2011) using

168   SHELXL2014/7 (Sheldrick 2015). Reflections showing anomalous calculated versus measured

169   structure factors; likely due to overlap with diamond and other phases in the multigrain sample,

170   resolution limitations, and volume of crystal illuminated by the X-ray beam, were omitted.

171   Structure models were visualized using Vesta (Momma and Izumi 2011) during the refinement

172   procedure.

3. RESULTS

173

174 *3.1 Synthesis and identification of Fe_5S_2 to 200 GPa*

175   Upon compression between 119(2) and 193(4) GPa and with heating to temperatures

176 between 2400–3300 K, the diffraction patterns are characterized by recrystallized of hcp-Fe and

177 diffuse streaks and sets of closely spaced reciprocal nodes suggestive of a complex atomic

178 arrangement of the coexisting sulfide (Figure 1, S1). With sustained heating, large sulfide grain

179 growth (3 – 6 µm) is observed (Figure 1). The diffraction angles for this synthesized sulfide

180 phase are not compatible with the Fe_3P-type Fe_3S at these conditions (Kamada et al., 2014).

181 Recrystallization of hcp-Fe with the sulfide crystallites at high temperatures was observed in all

182 experiments using the $Fe_{80}S_{20}$ and $Fe_{67}S_{33}$ starting powders as evidenced by the spotty (100) and

183 (101) hcp-Fe rings in Figure 1a. Fe recrystallization with this high-temperature Fe-sulfide

184 establishes that the probed sample locations were in a Fe-saturated phase field (Figure 1a) and

185 this sulfide phase is important to consider further in the context of Fe-rich planetary cores.

186   Upon temperature quenching in this pressure range, diffraction images were collected

187 while rotating the DAC across a +/- 17–30º range (depending on the DAC configuration). Grains

188 of a hexagonal lattice were identified in the reciprocal space with indexed parameters: $a =$

189 5.979(3) Å, $c = 11.088(6)$ Å at 140(2) GPa and 3070(180) K (Figure 1b, Table 1). However,

190 across the *P-T* explored, three polytypes were observed for this phase (Table 1). Each indexed

191 grain exhibits an *a* axial length of ~ 6 Å, while 3 differing *c* axial lengths are observed: ~ 11, 26,

192 and 73 Å. Diffraction mappings show that the polytypism is accompanied by diffuse scattering

193 along the *c* direction suggesting positional disorder along this axis (Figure S1). Decreased diffuse

194 scattering is observed after continued heating at peak temperatures in the KCl pressure media,

195   and grains with $a \sim 6$ Å, $c \sim 11$ Å were indexed (Figure 1b). This unit cell likely represents the

196   most positionally ordered arrangement relevant at these high P-T conditions.

197   The crystal structure of the Fe-sulfide synthesized at 140(2) GPa and 3070(180) K was

198   determined based on 159 observed reflections at these extreme conditions (Table 2). Assessment

199   of the systematic absences for the reduced structure factors suggests a $P6_3cm$ space group, and

200   structural solution and positional and displacement parameter refinement converged on an Fe_5S_2

201   compound adopting the Ni_5As_2 structure type (Table 2, 3; Figure 2) (Oryshchyn et al. 2011). The

202   measured unit cell parameters for this polytype are compatible with 6 formula units per cell

203   volume of Fe_5S_2. Furthermore, analogous polytypism due to stacking variations along the c

204   direction have been observed in related transition metal binary phases such as Pb_5As_2 (Saini et al.

205   1964). The diffraction angles and intensities measured in this study cannot be modeled based on

206   the tetragonal Fe_3S structure previously reported at these conditions (Kamada et al., 2012;

207   Ozawa et al., 2013; Mori et al., 2017).

208   The Ni_5As_2 structure that Fe_5S_2 adopts is a slight modification of the Pb_5Sb_2 structure (El-

209   Boragy et al. 1970), where the $M6$ site (M = metal) (Table 3) is split about its position given half

210   occupancy, changing its Wyckoff site from 6c to 12d (Figure 2) (Oryshchyn et al. 2011). A

211   significant improvement to the Fe_5S_2 refinement statistics was observed when incorporating the

212   disordered Fe6 site, suggesting that the Ni_5As_2 structure model better describes the Fe_5S_2

213   structure factors (Table 2). Displacement parameters for the Fe_5S_2 structure model were refined

214   as isotropic. Displacement parameters showing errors $> 3\sigma$ were fixed to a value equal to the

215   average displacement parameter value for Fe or S sites (Table 3). The isotropic displacement

216   parameter for the disordered Fe site was also fixed at an average Fe_{Uiso} value (Table 3). The

217   number of reflections collected at these extreme pressures limits the number of statistically

218 meaningful parameters to refine, and fixing displacement parameters to reasonable values

219 precludes overinterpretation of the current dataset. The high isotropic displacement parameter

220 observed on the Fe4 site may represent some vacancies on this site, but the dataset is again

221 deficient to refine site occupancies (Table 3).

222 A CIF file for the final Fe_5S_2 structure model is provided in Appendix A1. Following

223 previous descriptions of related M_5X_2 phases (e.g. Kjekshus et al. 1973; Oryshchyn et al. 2011),

224 Fe_5S_2 can be viewed as an arrangement of 6 Fe sites and 3 S sites with the Fe1, Fe2, Fe4, and

225 Fe6 sites in 13-fold coordination, the Fe3 and Fe5 sites in 12-fold coordination, and the S sites in

226 10-fold coordination (Figure 2c, Table 4). All sites are coordinated by both Fe and S sites.

227 Final R_1 values $\simeq$ 10% attest to the less-than ideal quality of the multigrain dataset as a

228 possible result of the 1-2 megabar synthesis conditions and observed c axial disorder and

229 stacking complexities in Fe_5S_2 (Table 2). Previous studies of isomorphic Ni_5As_2 and related

230 Pb_5As_2 at ambient conditions have also reported similar quality of refinements despite obtaining

231 significantly more reflections in the absence of a DAC (e.g. Saini et al. 1964; El-Boragy et al.

232 1970; Kjekshus et al. 1973). Notable challenges regarding the refinement of the Fe_5S_2 structure

233 model at these extreme conditions are discussed here and compared with similar difficulties

234 reported in previous characterizations of this structure type.

235 Thirteen violations of the $P6_3cm$ systematic absence condition: $l = 2n + 1$ for $(0kl)$, were

236 flagged during the refinement of Fe_5S_2. The reflections associated with these systematic absence

237 violations were examined in the raw diffraction images and show low, diffuse intensity.

238 Discrepancy over the presence or absence of weak reflections with $(0kl)$, $l=2n$ has been reported

239 in previous investigations of Ni_5As_2 and Pb_5As_2 (e.g. Saini et al. 1964; El-Boragy et al. 1970;

240 Kjekshus et al. 1973), suggesting that these studies also faced difficulties with space-group

241   determination. Observations of these low-intensity reflections could be a result of residual

242   disorder along the c direction, and longer heating cycles may be required for the atoms to arrange

243   into equilibrium positions. It is likewise possible that varying synthesis methods for Ni_5As_2 and

244   Pb_5As_2 in previous ambient condition studies affected the c axial atomic arrangement. Ni_5As_2

245   and isomorphic Ni_5P_2 also exhibits a homogeneity range of ~71.25 – 72.7 atomic % As

246   (Kjekshus et al. 1973; Litasov et al., 2019), and slight modifications of this structure based

247   stoichiometric and stacking variations result in trigonal structures such as $Ni_{31}Si_{12}$ (Frank and

248   Schubert 1971) and $(Fe, Ni)_8(Si, P)_3$ (perryite) (Okada et al. 1991). Attempts to refine the current

249   Fe-sulfide phase with the $Ni_{31}Si_{12}$ or perryite structure models did not significantly improve the

250   refinement statistics as the current high P-T dataset is too limited to resolve the intricacies that

251   differentiate these structures. Based on the presence of disorder, polytypism, anisotropic

252   vibrational motion, and nonstoichiometry in the related M_5X_2 phases, additional nuances to the

253   Fe_5S_2 structure model may be developed in future studies; however, the identification and

254   characterization of the Fe_5S_2 crystal structure determined here to 200 GPa is novel, and the

255   observations and challenges reported in this study align with that of previous analyses of Ni_5As_2

256   and Pb_5Sb_2 that were not affected by the limitations associated with performing microdiffraction

257   in a DAC at extreme conditions.

258

259   *3.2 Other sulfides observed during heating to 200 GPa and comparison of their structures with*

260   *Fe_5S_2*

261   X-ray diffraction from seven heating cycles performed between 100 and 200 GPa and to

262   3300 K provide insight into the Fe-rich Fe-S phase relations at outer core pressures and to high

263   temperatures. In each heating experiment, temperatures near melting were attained, and lattices

264 of Fe_5S_2 were indexed in the reciprocal space upon quenching. By further probing locations

265 across the thermal gradient of the laser heated spots, additional Fe-sulfides were characterized,

266 offering information on the lower temperature Fe-saturated sulfide crystal chemistries (Table 1,

267 2). These include Fe_3P-type Fe_3S (I-4, $Z = 8$), $C23$ Fe_2S (Co_2P-type, $Pnma$, $Z = 4$), and $C37$ Fe_2S

268 (Co_2Si-type, $Pnma$, $Z=4$), in lower temperature regions at 119 GPa, 131 GPa, and 140 GPa,

269 respectively (Figure 3; Table 1, 2).

270 Grains of tetragonal Fe_3S (I-4, $Z = 8$) (referred to herein as I-4 Fe_3S) were indexed with

271 parameters: $a = 8.094(3)$ Å, $c = 3.990(2)$ Å at 119(2) GPa, and refined to the Fe_3P-type structure

272 model (I-4, $Z = 8$) (referred to herein as I-4 Fe_3S), in agreement with previous studies (Fei et al.

273 2000; Seagle et al. 2006; Morard et al. 2007; Kamada et al. 2010; Kamada et al. 2012;

274 Thompson et al. 2020) (Table 2, Figure 3a, Appendix A2). The structure can be viewed as

275 containing 3 tetrahedrally coordinated Fe sites (Blanchard et al. 2008): one Fe-site is coordinated

276 only by S atoms with an average bond length of 2.083(9) Å, another Fe site is coordinated by 3 S

277 atoms and 1 Fe atom with an average bond length of 2.146(8) Å, and the third Fe site is

278 coordinated by 2 S and 2 Fe atoms with an average bond length of 2.137(8) Å (Figure 3). The

279 measured interatomic distances are comparable to reports on other transition metal M_3X

280 structures (e.g. Aronnson 1955; Rundqvist 1979).

281 After heating at 131(2) GPa, grains of Fe_3S were not observed across the heated spot.

282 Instead, orthorhombic lattices were also identified with parameters $a = 4.869(2)$ Å, $b = 3.256(2)$

283 Å, $c = 6.139(2)$ Å, compatible with 4 formula units of Fe_2S. Structural solution and refinement

284 indicate that the Fe_2S grains adopt the $C23$ structure (Co_2P type, $Pnma$, $Z = 4$) in agreement with

285 previous structural analyses at lower pressures (Zurkowski et al. *in press*) (Table 2, Figure 3b,

286 Appendix A3). The structure is composed of columns of FeS_4 tetrahedra and columns of FeS_5

287   square pyramids linked along edges in the *b* direction (Figure 3b). The average Fe–S bond

288   lengths are 2.213(8) Å and 2.011(2) Å in the square pyramids and tetrahedra, respectively. These

289   values are comparable with those observed in $C23$ Fe_2S at 90 GPa (Zurkowski et al. *in press*).

290   Upon temperature quenching at 140(2) GPa, orthorhombic grains were identified in the

291   sample chamber with a = 4.667(2) Å, 3.289(1) Å, 6.186(4) Å. This unit cell is similar to the $C23$

292   Fe_2S cell measured at 130 GPa, but it exhibits a 4 % contraction of the *a* axial length, a 1%

293   extension of the *b* and *c* axial lengths, and a 2% volume decrease. Structure solution and

294   refinement establishes that Fe_2S adopts the $C37$ structure (Co_2Si-type, *Pnma, Z*=4) (Table 2,

295   Figure 3c, Appendix A4). This result confirms the previously proposed $C23$–$C37$ transition in

296   Fe_2S at these conditions and presents a comparable volume change (Zurkowski et al., *in press*).

297   Inherent to the $C23$–$C37$ transition is coordination change from the 4-fold Fe1 coordination

298   polyhedra in the $C23$ structure to the 5-fold dipyramid polyhedra in the $C37$ structure (Figure 3b,

299   c). Comparing the $C23$ and $C37$ structure models determined at 130 and 140 GPa, respectively, a

300   10% contraction of the interatomic distance involved in the coordination change is observed

301   (Figure S2). The average Fe–S bond lengths measured in $C37$ Fe_2S are 2.196(2) Å and 2.165(3)

302   Å in the square pyramids and dipyramids, respectively. These values are comparable with those

303   observed in $C23$ Fe_2S in this study.

304   Comparison of the interatomic distances and coordination environments in the Fe-

305   sulfides observed in this study distinguishes Fe_5S_2 as particularly unique among them. Within an

306   interatomic distance of 2.7 Å (Table 4, Appendix A1-A4), $C23$ and $C37$ Fe_2S consist of Fe sites

307   coordinated only by S, while Fe_3S and Fe_5S_2 mark a drastic increase in Fe-Fe bonding with Fe

308   surrounded by up to 9 Fe sites in both structures. However, Fe_5S_2 exhibits Fe-Fe bond lengths up

309   to 25% shorter than that observed in Fe_3S at these pressures, further distinguishing the increased

310   iron-iron interactions in the novel Fe_5S_2 at Earth and planetary core pressures (Figure 2c, Table

311   4).

312

313   *3.3 Fe-rich sulfide phase relations at core-mantle boundary pressures*

314   The presented single-crystal derived structures of Fe_5S_2, Fe_3S, $C23$ Fe_2S and $C37$ Fe_2S

315   were then used to inform the changes in diffraction patterns collected during heating between

316   110 and 200 GPa and to ~3250 K (Figure 4). Beginning at 112 GPa, diffraction signal from $C23$

317   Fe_2S coexisting with Fe was first identified upon heating of the $Fe_{80}S_{20}$ starting material to

318   ~2000 K (Figure 4). With continued heating, peaks associated with tetragonal Fe_3S were

319   observed over a limited temperature range ($\lesssim$ 2400 K) until diffuse scattering signal and Bragg

320   reflections from Fe_5S_2 first appeared. Crystallization of the Fe_5S_2 grains with hcp-Fe occurred

321   with continued heating to 119(2) GPa and 2840(180) K (Figure 4).

322   Upon heating beginning at 120 GPa, $C23$ Fe_2S was observed coexisting with Fe to 122(1)

323   GPa and 2290(120) K, above which the onset of diffraction from the Fe_5S_2 phase was identified

324   and Fe_5S_2 crystallites formed coexisting with hcp-Fe to 131(2) GPa and 3050(140) K (Figure 4).

325   I-4 Fe_3S was not observed. With continued heating cycles between 133(1) GPa and 194(2) GPa

326   and up to 3250 K, $C37$ Fe_2S coexists with Fe at moderate temperatures and a reaction to form

327   Fe_5S_2 occurs at high temperatures (Figure 4). A pressure-induced $C23$–$C37$ Fe_2S transition is

328   therefore constrained between 125 and 135 GPa, in agreement with previous investigations of

329   Fe_2S (Zurkowski et al. *in press*).

4. DISCUSSION

4.1 Discrepancies among the current and previous studies

330

331

332   Transitional metal binary compounds with metal-to-nonmetal ratios ranging from 2.33–

333   2.66 (~70–73 atm% metal) predominantly adopt complex trigonal or hexagonal structures with

334   considerable metal-metal bonding (Chen and Whitmire 2018 and references therein). Our

335   observations of the disorder, polytypism, and complex coordination environments inherent to

336   Fe_5S_2 demonstrate that it aligns with this systematic characterization. Interestingly, this work

337   elucidates that the Fe_5S_2 atomic arrangement is thermodynamically favored and expresses greater

338   Fe-Fe interactions at the extreme conditions of Earth's outer core compared to that of *I*-4 Fe_3S.

339   These results are contrary to previous reports of Fe_3S stability on to high temperatures in

340   Fe-rich systems to 250 GPa (Kamada et al. 2010; Kamada et al. 2012; Ozawa et al. 2013; Mori et

341   al. 2017), but our observations may account for these discrepancies. First, interpretation of Fe_5S_2

342   in the integrated powder diffraction patterns is difficult due to the variation in diffraction signal

343   obtained from the Fe_5S_2 polytypes and the low intensity scattering from the disordered sites

344   during its formation (Figure S1, S3). Fe_5S_2 also forms large crystallites, limiting the orientations

345   of the phase and rendering indexation of all diffraction angles for Fe_5S_2 quite challenging

346   without rotating the sample (Figure 1a). The implementation of single-crystal X-ray diffraction

347   techniques at high pressures was critical in the current study to accurately characterize the

348   hexagonal unit cell geometry and complex structure of the Ni_5As_2-like Fe_5S_2 and to constrain the

349   stability field of *I*-4 Fe_3S.

350   Several studies have also reported chemically analyzed Fe_3S grains in samples recovered

351   from high temperatures in the 200–250 GPa range (Mori et al. 2017; Yokoo et al. 2019; Ozawa

352   et al. 2013), but the difference in Fe content between Fe_3S and Fe_5S_2 may be as few as 3%. This

353   value is generally within 3σ uncertainty reported for chemical analyses of samples recovered

354   from these extreme conditions, posing another challenge for distinguishing between the synthesis

355   of Fe_3S and Fe_5S_2. Furthermore, based on characterizations of the isomorphic Ni_5As_2 and Ni_5P_2,

356   these structures exhibit a homogeneity range with up to ~73 atm% metal (Kjekshus et al. 1973;

357   Litasov et al., 2019). TEM analysis of a Fe–S sample recovered from 236 GPa and 2980 K

358   reveals sulfide grains with on average ~73 atm% Fe (Ozawa et al. 2013); this value is within

359   0.3–1.25 atom % of the possible range of Fe_5S_2 stoichiometries and 2 atomic percent less than an

360   Fe_3S composition. The results from previous chemical analyses of samples recovered from outer

361   core pressures and high temperatures (Mori et al. 2017; Yokoo et al. 2019; Ozawa et al. 2013)

362   therefore do not contradict the current results, and simply indicate previous misinterpretation of

363   Fe_5S_2 as Fe_3S, based on EDS measurements alone, in the absence of single-crystal diffraction

364   analysis.

365

366   *4.2 Sulfur in Earth and Planetary cores*

367   The stability of Fe_5S_2 and the phase relations observed in this study present novel

368   constraints on the material properties of Fe-sulfides at conditions relevant to Earth's outer core,

369   Venus' core, and exoplanetary cores of similar size and core-mass fraction (CMF). Namely, at

370   pressures ≥120 GPa, Ni_5As_2-type Fe_5S_2, not tetragonal Fe_3S as previously believed, is the

371   relevant Fe-rich sulfide. As Earth's outer core crystallizes over time, Fe_5S_2 will eventually

372   crystallize over a large depth range up to the CMB. Tetragonal Fe_3S has been confirmed to 120

373   GPa (Figure 4) (Seagle et al. 2006; Morard et al. 2008; Thompson et al., 2020), constraining the

374    $Fe_3S + Fe \rightarrow Fe_5S_2 + Fe$ transition to ~120 GPa. Rocky planetary bodies with sizes and CMFs

375   like that of Venus (CMB = 114 GPa) (Aitta 2012) would likely crystallize Fe_3S at the CMB, but

376   Fe_5S_2 will be crystallizing over much of the core's depth. $C37$ Fe_2S is reported to be stable on the

377   solidus above 306 GPa in Fe-rich systems (Tateno et al. 2019), suggesting a $Fe_5S_2 + Fe \rightarrow Fe_2S$

378    $+ Fe$ transition in the 200–300 GPa range. $C37$ Fe_2S remains the candidate Fe-rich sulfide at

379   Earth's ICB, but for planets like Venus with a central pressure of 274 GPa (Aitta 2012), Fe_5S_2

380   may instead be the relevant Fe-rich sulfide, necessitating experimental determination of the

381    $Fe_5S_2 \rightarrow Fe_2S + Fe$ decomposition P-T boundary. Furthermore, as Fe_5S_2 exhibits a complex

382   crystalline arrangement with increased metal-metal bonding compared to Fe_2S and Fe_3S at core

383   pressures, the significant depth over which Fe_5S_2 crystallizes in and Venus- to Earth-sized

384   planetary cores may also contribute to higher conductivity signatures in these regions.

385   The stability of Fe_5S_2 coexisting with Fe between 120 and 200 GPa to to 3250 K also

386   requires a change in melting behavior associated with the change in solidus phase from I-4 Fe_3S

387   to Fe_5S_2 above 120 GPa. As Fe_5S_2 is observed to temperatures of ~3250 K, a kink in the Fe-

388   sulfide solidus curve (Mori et al. 2017) is proposed to accommodate this (Figure 7). Further

389   work examining melt signal will be helpful for accurately determining the shape of the solidus

390   curve above 120 GPa, but the disorder observed in Fe_5S_2 may challenge the determination of

391   melting that is commonly based on diffuse scattering appearing in the diffraction background.

392   Further changes in melting relations occur as $C37$ Fe_2S becomes stable to melting temperatures

393   above 306 GPa, and future experiments must investigate the change in melting temperatures

394   associated with this transition at lower outer core conditions.

395   Terrestrial core chemistries are multicomponent; Si and Ni are also important core-

396   alloying elements in planets such as Earth, drawing attention to the potential stability of the

397   perryite (Fe, Ni)$_8$(Si, P)$_3$ structure in (Fe, Ni) – (Si, S)-rich cores. Perryite, observed in enstatite

398   chondrites and aubrites, adopts a trigonal stacking variant of the Ni_5As_2-type structure (Wasson

399 and Wai, 1970; Okada et al. 1991), and iron phosphides tend to adopt analog structures to those

400 observed in iron sulfides (i.e., Fei et al. 2000; Dera et al. 2008; Gu et al. 2014; Gu et al. 2016;

401 Zurkowski et al., in press). Hence, Fe_5S_2 could potentially serve as a host for nickel and silicon

402 in its perryite-like structure at Earth's outer core conditions. Furthermore, Si has recently been

403 shown to dissolve into iron-sulfide phases and expand their stability field to higher pressure (Tao

404 and Fei, 2021). The dissolution of silicon into Fe_5S_2 may expand its stability to higher pressures,

405 making it potentially relevant at Earth's ICB conditions. If this is the case, the partitioning of Si

406 and Ni between $(Fe, Ni)_5(S, Si)_2$ and (Fe, Ni, Si) and the density difference between the inner-

407 core-crystallizing phase and remaining light-element-rich liquid will be crucial to investigations

408 of the inner-core-density deficit and inner core seismic morphology.

409

5. CONCLUSIONS

411   To assess the phase stability of Fe-rich sulfides at Earth's outer core conditions, Fe-rich

412 sulfide compositions were examined to 200 GPa and 3250 K using single-crystal and powder X-

413 ray diffraction techniques in a laser-heated diamond anvil cell. At high temperatures between

414 120 and 200 GPa Fe_5S_2 is synthesized in the Ni_5As_2-type structure. The atomic arrangement of

415 this hexagonal structure is characterized by positional disorder, complex coordination

416 environments and significant Fe-Fe interactions. Additional polytypism and disorder associated

417 with various stacking arrangements along the c direction are also observed. Along with Fe_5S_2,

418 grains of I-4 Fe_3S, C23 Fe_2S, and C37 Fe_2S were also characterized. The stability of tetragonal

419 Fe_3S in Fe-rich systems is constrained to below 120 GPa. C23 Fe_2S + Fe is observed at moderate

420 temperatures to 130 GPa, and C37 Fe_2S + Fe is observed at moderate temperatures above 140

421 GPa. Between 120 and 200 GPa at the highest temperatures probed, Fe_5S_2 is stable coexisting

422 with Fe, therefore establishing that Fe_5S_2, not Fe_3S, is stable in Fe-rich systems at outer core

423 pressures associated with Earth- and Venus-sized bodies. Fe_5S_2 crystallization can be expected

424 over a extensive depth range in the cores of these planetary bodies.

425

Acknowledgments

6. TABLES

Table 1. Unit cell parameters of Fe_5S_2, Fe_3S, and Fe_2S measured upon quenching from high *P-T* synthesis in this study. Each cell was indexed in the reciprocal space, and the DAC opening, and number of reflections obtained for each lattice are listed. For select experiments, high-temperature synthesis was conducted without collecting X-ray diffraction data, and the synthesis conditions for these experiments are listed as "high T, not measured."

| | | | Room temperature collection | | | | | | | | Synthesis conditions | |
| | Starting | | Phase | P | a | b | c | V | DAC opening | no. of reflections | P | T |
Sample name	material	medium		GPa	Å	Å	Å	Å^3	(°)		GPa	K
C140_P2_map25	Fe80S20	KCl	Fe5S2	105(2)	6.020(4)		11.204(7)	351.6(5)	60	290	119(2)	2840(140)
C140_P2_map31	Fe80S20	KCl	Fe5S2	105(2)	6.050(2)		73.0(2)	2313(1)	60	134	119(2)	2840(140)
C140_P4_map10	Fe80S20	KCl	Fe5S2	118(1)	5.983(3)		11.078(6)	343.4(4)	60	489	140(2)	3070(180)
C140_P4_map14	Fe80S20	KCl	Fe5S2	118(1)	5.979(2)		11.084(4)	343.2(3)	60	379	140(2)	3070(180)
C140_P4_map14	Fe80S20	KCl	Fe5S2	118(1)	5.973(1)		11.094(2)	342.8(1)	60	276	140(2)	3070(180)
C129_P140_map71	Fe67S33	SiO2	Fe5S2	136.4(5)	5.957(4)		71.89(4)	2209(3)	34	84	159(2)	3230(150)
C129_P150_map9	Fe67S33	SiO2	Fe5S2	144.2(8)	5.939(3)		25.99(6)	794(2)	34	76	high T, not measured	
C129_P150_map9	Fe67S33	SiO2	Fe5S2	144.2(8)	5.923(1)		26.004(6)	789.9(3)	34	146	high T, not measured	
C137_P1_map25	Fe80S20	SiO2	Fe5S2	159(1)	5.890(3)		25.837(7)	776.2(5)	40	108	184(3)	3250(260)
C137_P1_map25	Fe80S20	SiO2	Fe5S2	159(1)	5.880(1)		25.789(3)	772.0(2)	40	108	184(3)	3250(260)
C137_P1_map25	Fe80S20	SiO2	Fe5S2	159(1)	5.876(2)		25.884(8)	774.0(4)	40	116	184(3)	3250(260)
C137_P1_map25	Fe80S20	SiO2	Fe5S2	159(1)	5.883(3)		25.85(1)	774.6(7)	40	126	184(3)	3250(260)
C137_P1	Fe80S20	SiO2	Fe5S2	159(1)	5.897(3)		25.90(1)	775.1(6)	40	116	184(3)	3250(260)
C137_P1	Fe80S20	SiO2	Fe5S2	159(1)	5.878(1)		25.784(3)	771.6(2)	40	149	184(3)	3250(260)
C137_P2_34	Fe80S20	SiO2	Fe5S2	179(1)	5.8400(7)		25.583(2)	755.7(1)	40	189	193(4)	3010(160)
C140_P1_map	Fe80S20	KCl	Fe3S	100(1)	8.156(3)		4.025(3)	267.8(3)	60	416	high T, not measured	
C140_P2_map25	Fe80S20	KCl	Fe3S	105(2)	8.094(3)		3.990(2)	261.4(2)	60	296	119(2)	2840(140)
C140_P3_map6	Fe80S20	KCl	*C*23Fe2S	111(1)	4.869(2)	3.256(2)	6.139(2)	97.3(1)	60	227	131(2)	3050(140)
C140_P4_map10	Fe80S20	KCl	*C*37 Fe2S	118(1)	4.677(2)	3.289(1)	6.186(4)	95.18(9)	60	188	140(2)	3070(180)

442
443
444
445
446
447
448
449
450
451
452
453
454
455
456

457 **Table 2.** Select experimental details for crystal structure synthesis and analysis of Fe_5S_2, Fe_3S,
458 and the Fe_2S polymorphs.

Phase	Fe_5S_2	Fe_3S	*C*23 Fe_2S	*C*37 Fe_2S
Sample Name	**C140_P4_map10**	**C140_P2_map25**	**C140_P3_map6**	**C140_P4_map10**
Synthesis				
Pressure (GPa)	140(2)	119(2)	131(2)	140(2)
Synthesis Temperature (K)	3070(180)	2840(140)	2050(140)	3070(180)
Symmetry	Hexagonal, *P*6(3)*cm*, Z=6	Tetragonal, *I*-4, Z=8	Orthorhombic, *Pnma*, Z = 4	Orthorhombic, *Pnma*, Z = 4
a (Å)	5.979(2)	8.094(3)	4.869(3)	4.677(2)
b (Å)			3.256(4)	3.289(1)
c (Å)	11.087(6)	3.990(2)	6.139(2)	6.186(4)
V (Å^3)	343.2(3)	226.4(2)	97.3(1)	95.18(9)
Reduction				
No. of measured, independent and observed [$I > 2\sigma(I)$] reflections	396, 309, 157	332, 314, 219	227, 208, 112	188, 158, 105
R_{int}, R_{sigma}	0.092, 0.062	0.053, 0.072	0.012, 0.016	0.009, 0.014
Refinement				
$R[F^2 > 2\sigma(F^2)]$, $wR(F^2)$, S	0.098, 0.255, 1.12	0.067, 0.164, 1.05	0.053, 0.149, 1.21	0.047, 0.139, 1.22
No. of reflections	156	219	112	105
No. of parameters	21	17	10	10
$\Delta\rho_{max}$, $\Delta\rho_{min}$ (e Å^{-3})	2.14, -2.18	1.92, -1.68	1.86, -2.02	1.91, -2.21

459
460
461
462
463

464 **Table 3.** Atomic coordinates of the Fe_5S_2 refinement model for the data collected at 140(2) GPa
465 and quenched from 3070(180) K.

Wycoff site	ATOM	x	y	z	Uiso
2a	Fe1	0	0	0.963	0.021
	error			0.003	0.005
4b	Fe2	1/3	2/3	0.089	0.046
	error			0.003	0.005
6c	Fe3	0.259	0	0.126	0.021
	error	0.002		0.001	
6c	Fe4	0.613	0	0.222	0.021
	error	0.002		0.001	0.003
6c	Fe5	0.284	0	0.330	0.027
	error	0.002		0.001	0.003
12d	Fe6*	0.651	0.056	0.426	0.021
	error	0.003	0.003	0.002	
2a	S1	0	0	0.220	0.026
	error			0.004	
4b	S2	1/3	2/3	0.299	0.026
	error			0.002	
6c	S3	0.673	0	0.030	0.026
	error	0.005		0.003	

*indicates half occupancy

466
467
468
469
470
471
472
473
474
475
476
477
478

479 **Table 4.** Selected interatomic distances for the Fe sites measured in Fe_5S_2 at 140 GPa. The "#"
480 column indicates that number of the "bonded to" sites around the central atom.

Atom	bonded to	#	distance (Å)
Fe1	–Fe3	3	2.39(2)
	–Fe5	3	2.22(3)
	–Fe6	3	2.313(17)
	–S1	1	2.66(8)
	–S4	3	2.09(3)
Fe2	–Fe3	3	2.275(3)
	–Fe4	3	2.375(16)
	–Fe6	3	2.40(3)
	–S3	1	2.36(4)
	–S4	3	2.108(13)
Fe3	–Fe1	1	2.39(2)
	–Fe2	2	2.275(8)
	–Fe4	3	2.350(15)
	–Fe5	1	2.30(3)
	–Fe6	1	2.307(17)
	–S1	1	1.90(4)
	–S4	3	2.68(3)
Fe4	–Fe2	2	2.375(16)
	–Fe3	3	2.320(11)
	–Fe5	3	2.416(14)
	–Fe6	1	2.303(17)
	–S1	1	2.326(11)
	–S3	2	2.044(16)
	–S4	1	2.10(3)
Fe5	–Fe1	1	2.22(3)
	–Fe3	1	2.30(3)
	–Fe4	3	2.416(14)
	–Fe6	3	2.135(15)
	–S1	1	2.09(5)
	–S3	2	2.184(10)
	–S4	1	2.27(3)
Fe6	–Fe1	1	2.313(17)
	–Fe2	2	2.40(3)
	–Fe3	1	2.307(17)
	–Fe4	1	2.303(17)
	–Fe5	3	2.135(15)
	–S3	2	2.15(3)
	–S4	3	2.17(3)

481

482

483 **Figures**
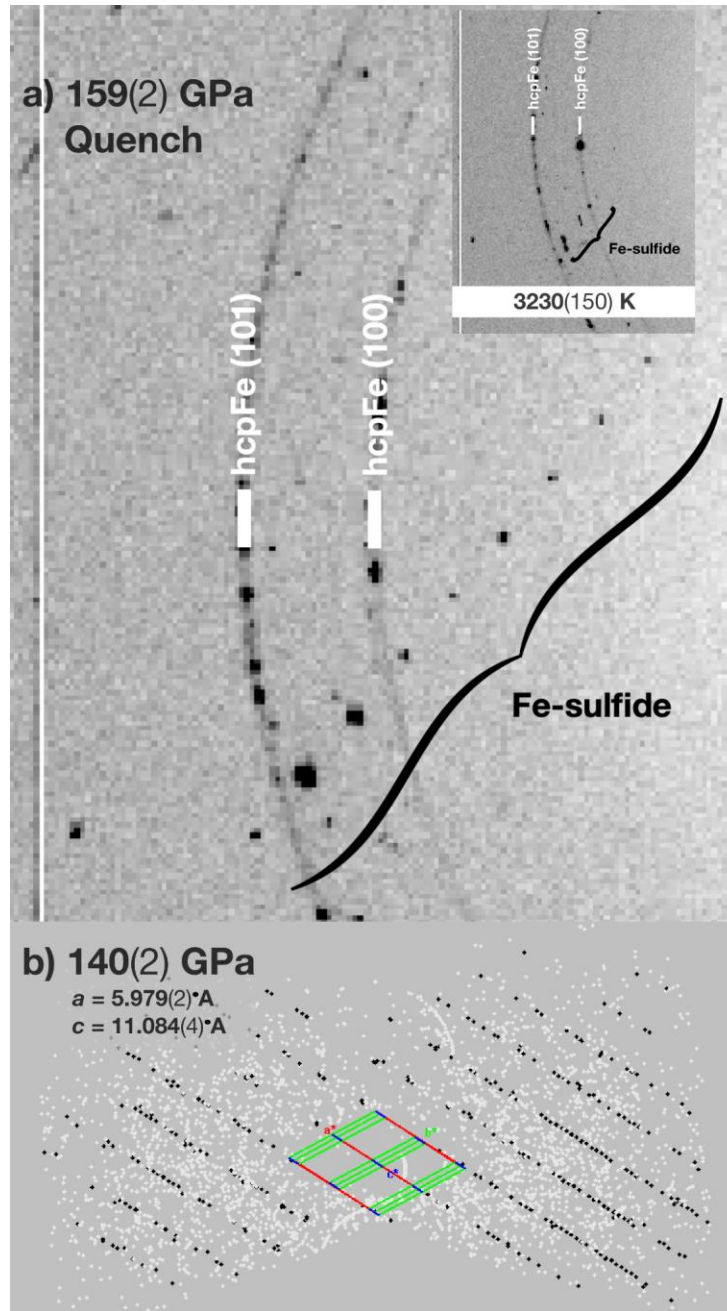
484

485 **Figure 1.** a) View of a crystallite of the high-temperature Fe_5S_2 coexisting with recrystallized
486 hcp-Fe after synthesis at 159(2) GPa and 3230(130) K (inset). The spotty rings corresponding to
487 the hcp-Fe (100) and (101) planes demonstrate that iron equilibrated at 159(2) GPa and
488 3230(130) K. b) View of the reciprocal space for reflections detected in an experiment on the
489 $Fe_{80}S_{20}$ composition quenched from 140(2) GPa and 3070(140) K. The reciprocal lattice, colored
490 in black, is associated with a Fe_5S_2 grain whose lattice parameters are provided in the top left.
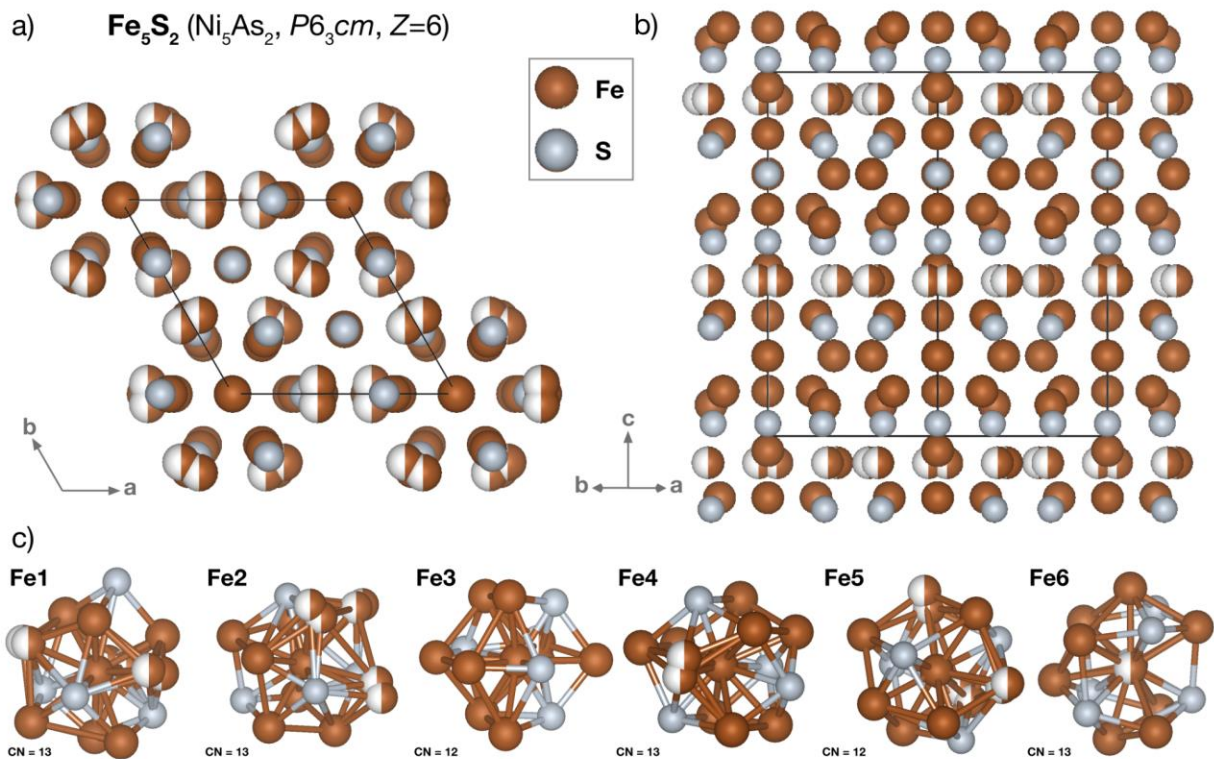
Figure 2. Crystal structure of Fe_5S_2 viewed along the a) *c* axis and the b) (100) plane. c) The Fe-coordination polyhedra observed in this atomic arrangement are provided. Fe1, Fe2, Fe4, and Fe6 are coordinated by 13 sites and Fe3 and Fe5 are coordinated by 12 sites. Each coordination polyhedron consists of Fe and S sites.

a) **Fe₃S** (Fe₃P-type, *I*-4, *Z* = 8)

b) **C23 Fe₂S** (Co₂P-type, *Pnma*, *Z* = 4)

c) **C37 Fe₂S** (Co₂Si-type, *Pnma*, *Z* = 4)
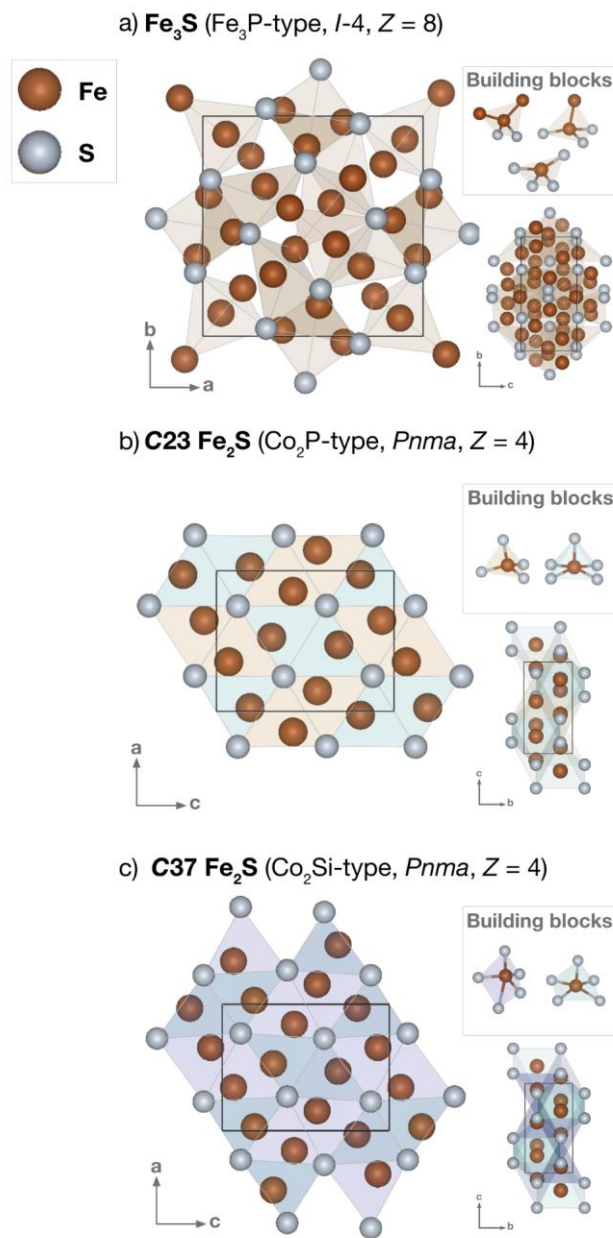
496
497   **Figure 3.** Crystal structures of Fe₃S and Fe₂S observed in this study. a) Fe₃S adopts the Fe₃P-
498   type structure (*I*-4, *Z* = 8) that is composed of three tetrahedrally coordinated Fe-sites, each with
499   increasing Fe–Fe bonding. b) The *C*23 Fe₂S structure (Co₂P-type, *Pnma*, *Z* = 4) is made up of
500   columns of FeS₄ tetrahedra and columns of FeS₅ square pyramids linked along edges in the *b*
501   direction. c) The *C*37 Fe₂S structure (Co₂Si-type, *Pnma*, *Z* = 4) has the same site symmetries as
502   the *C*23 structure, but is marked by a shortened *a* axis and elongated *b* and *c* axes accompanied
503   by the formation of a 5-fold dipyramid.
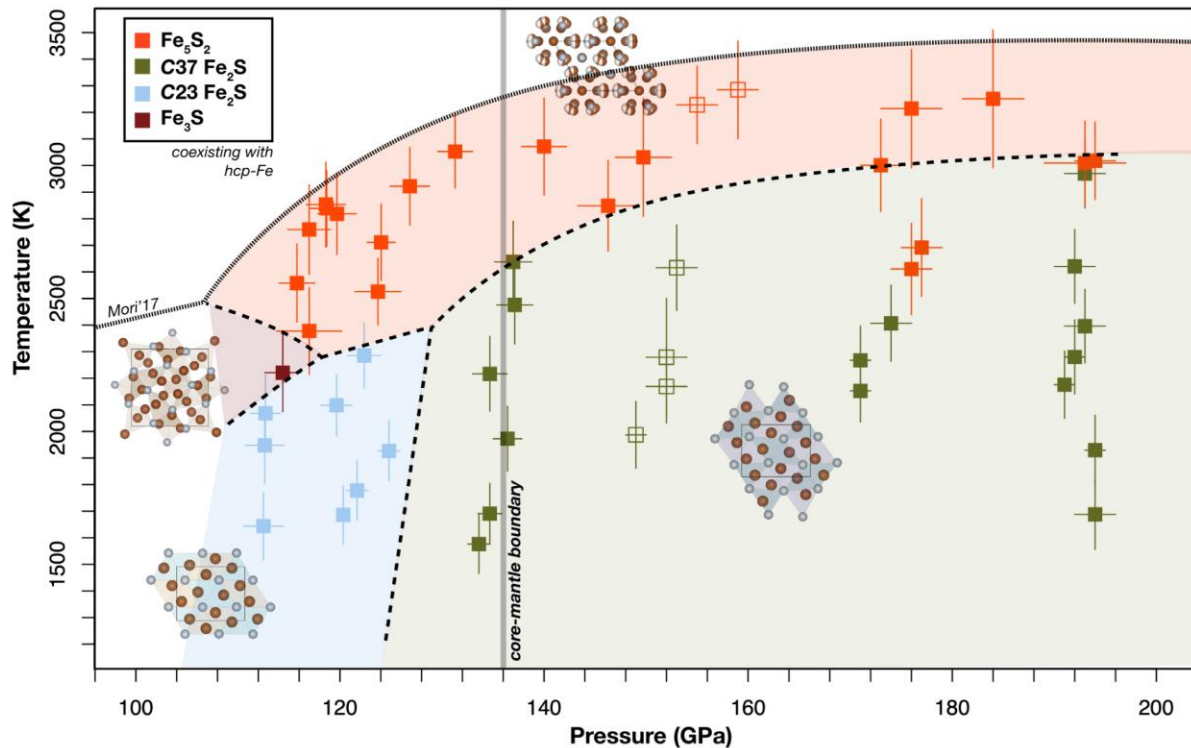
Figure 4. The single-crystal derived structures of Fe_5S_2, Fe_3S, and Fe_2S were then used to interpret the diffraction patterns collected during heating (Figure S3). At moderate temperatures, Fe_3S is observed below 120 GPa, $C23$ Fe_2S is observed below 130 GPa, and $C37$ Fe_2S is observed above 130 GPa. At high temperatures to 200 GPa, Fe_5S_2 is stable, and a kink in the Fe-S solidus curve (Mori et al., 2017) is presented to account for the change from Fe_3S to Fe_5S_2 melting in Fe-rich systems above ~120 GPa. The closed squares represent experiments conducted on the $Fe_{80}S_{20}$ starting material, and the open squares represent experiments conducted on the $Fe_{67}S_{33}$ starting material. Both show compatible results and iron recrystallization at high temperatures, indicating that Fe-rich regions of the $Fe_{67}S_{33}$ foils were probed.

8. SUPPLEMENTAL

Figure S1. Unwarped diffraction mappings of the (1kl), (0kl), and (-1kl) directions for an Fe_5S_2 crystallite exemplifying the diffuse scattering signal collected at 119(2) and 2840(180) K. The (1kl) and (-1kl) mappings also show the presence of a polytype with more closely spaced reflections oriented ~51° from the mapped crystallite.
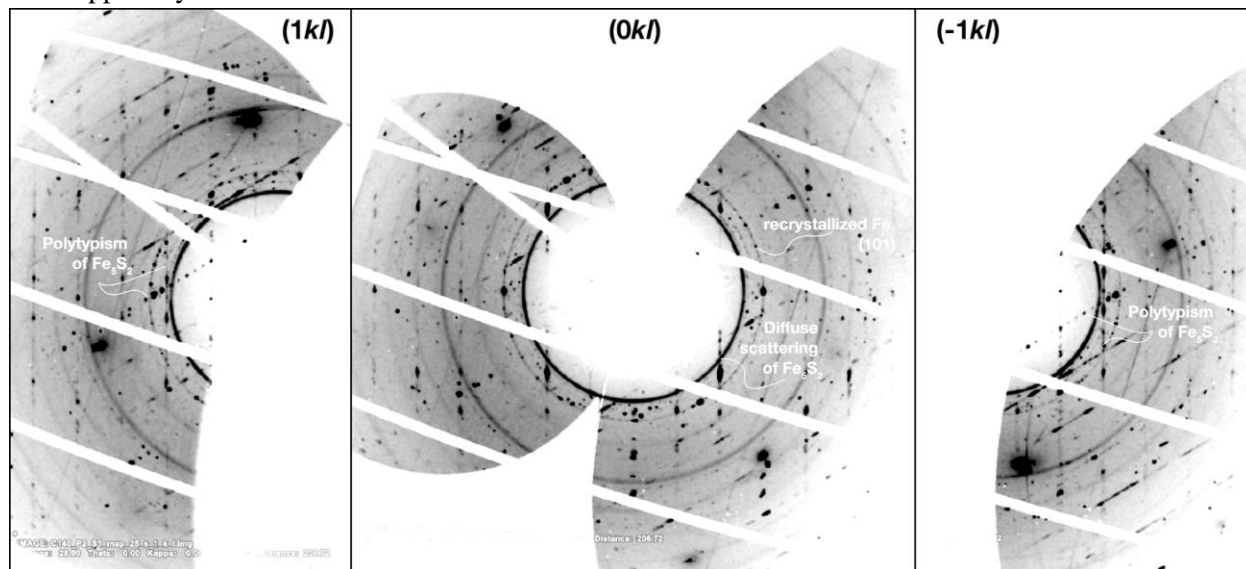
551   **Figure S2.** Comparison of the $C23$ and $C37$ Fe_2S structure models refined at 130 and 140 GPa,
552   respectively. In the $C23$ Fe_2S structure, the next nearest sulfur site to the Fe1 tetrahedral site is at
553   a 2.963(1) Å distance at 130 GPa (dotted line). A 10% contraction of this interatomic distance
554   and a coordination change is observed in the formation of $C37$ Fe_2S at 140 GPa (right).
555

C23 Fe$_2$S (Co$_2$P-type, *Pnma*, $Z = 4$)   **C37 Fe$_2$S** (Co$_2$Si-type, *Pnma*, $Z = 4$)

556
557
558
559
560
561
562
563
564
565
566
567
568
569
570
571
572
573
574
575
576
577
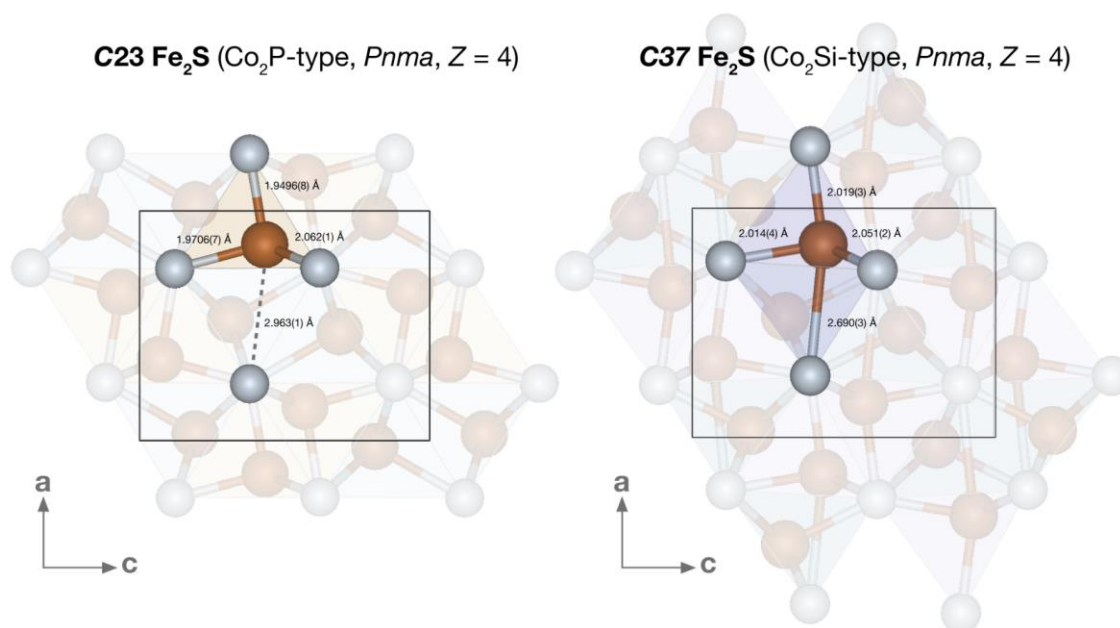
Figure S3. X-ray diffraction patterns collected upon heating in an $Fe_{80}S_{20}$ starting composition at a) 119(2) GPa and b)184(3) GPa. The miller indices for $C23$ Fe_2S (blue), Fe_3S (burgundy), and $C37$ Fe_2S (green) are provided, and the red "H" symbols represent the observations of the formation of Fe_5S_2. The growth of large crystallites, along with the disorder and polytypism of this phase make for challenging powder diffraction indexing, but the lattice parameters of Fe_5S_2 indexed in the reciprocal space after quenching from these high P-T conditions are provided.
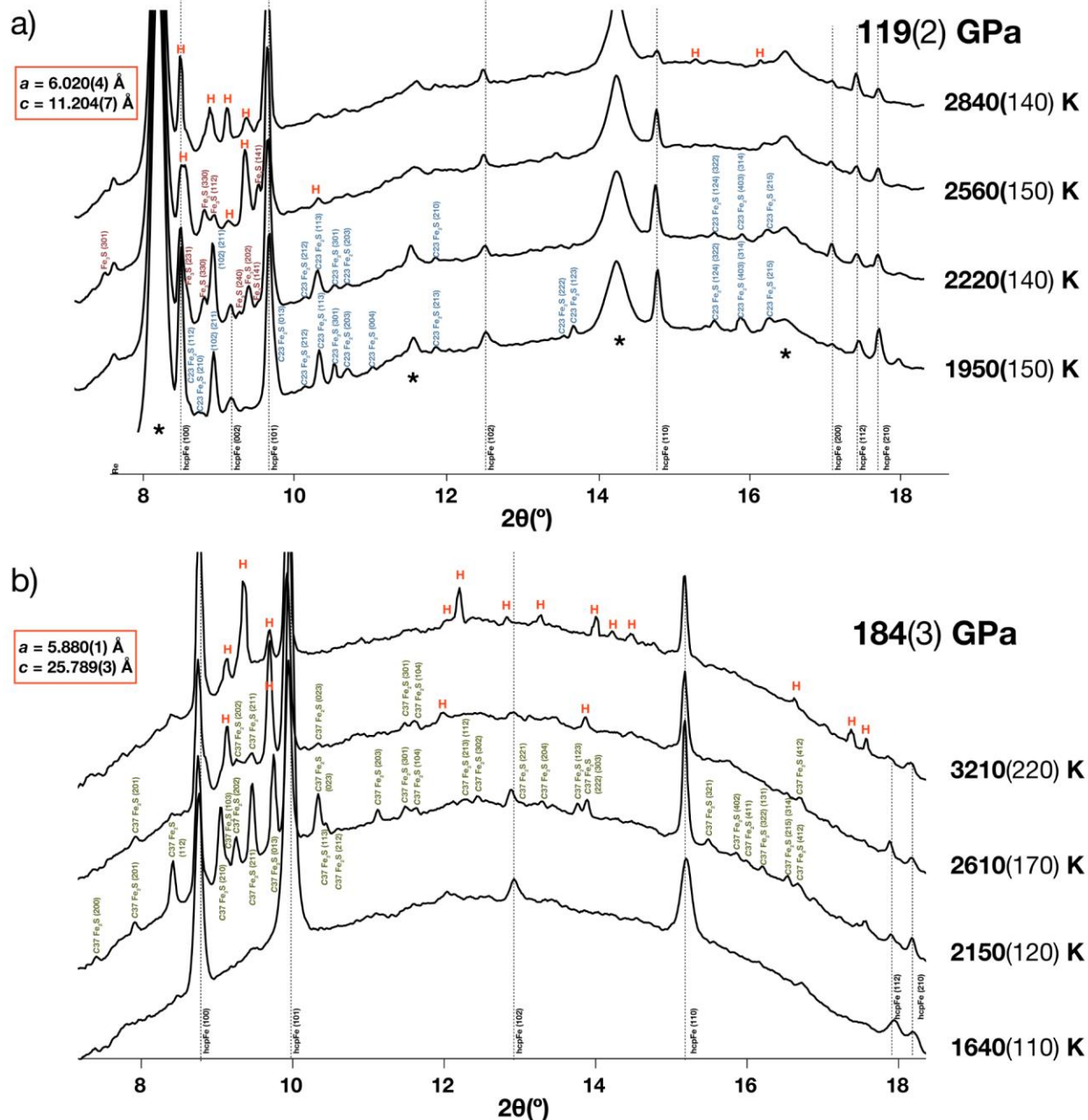
References

587 **References**

588 Anzellini, S., Dewaele, A., Mezouar, M., Loubeyre, P. and Morard, G., 2013. Melting of iron at
589   Earth's inner core boundary based on fast X-ray diffraction. Science, 340, 464–466.
590   https://doi.org/10.1126/science.1233514

591 Birch, F., 1952. Elasticity and constitution of the Earth's interior. J. Geophys. Res., 57, 227–286.
592   https://doi.org/10.1029/JZ057i002p00227

593 Campbell, A.J., Seagle, C.T., Heinz, D. L., Shen, G., and Prakapenka, V.B., 2007. Partial
594   melting in the iron-sulfur system at high pressure: A synchrotron X-ray diffraction study.
595   Phys. Earth Planet. Inter., 162, 119–128. https://doi.org/10.1016/j.pepi.2007.04.001

596 Campbell, A.J., Danielson, L., Righter, K., Seagle, C.T., Wang, Y. and Prakapenka, V.B., 2009.
597   High pressure effects on the iron–iron oxide and nickel–nickel oxide oxygen fugacity
598   buffers. Earth Planet. Sci. Lett., 286, 556–564. https://doi.org/10.1016/j.epsl.2009.07.022

599 Chen, J.H. and Whitmire, K.H., 2018. A structural survey of the binary transition metal
600   phosphides and arsenides of the d-block elements. Coord. Chem. Rev., 355, 271–327.
601   https://doi.org/10.1016/j.ccr.2017.08.029

602 Dewaele, A., Loubeyre, P., Occelli, F., Mezouar, M., Dorogokupets, P.I. and Torrent, M., 2006.
603   Quasihydrostatic equation of state of iron above 2 Mbar. Phys. Rev., 97, 215504.
604   https://doi.org/10.1103/PhysRevLett.97.215504

605 Dziewonski, A.M. and Anderson, D.L., 1981. Preliminary reference Earth model. Phys. Earth
606   Planet. Inter., 25, 297–356. https://doi.org/10.1016/0031-9201(81)90046-7

607 El-Boragy, M., Bhan, S. and Schubert, K., 1970. Kristallstruktur von Pd_5Sb_2 und Ni_5As_2 und
608   einigen varianten. J. less-common met, 22, 445–458.
609   https://doi.org/10.1016/0022-5088(70)90132-3

610 Evans, H.T., 1970. Lunar troilite: crystallography. Science, 167, 621–623.
611   https://doi.org/10.1126/science.167.3918.621

612 Fearn, D.R. and Loper, D.E., 1981. Compositional convection and stratification of Earth's core.
613   Nature, 289, 393–394. https://doi.org/10.1038/289393a0

614 Fei, Y., Prewitt, C.T., Mao, H.K. and Bertka, C.M, 1995. Structure and density of FeS at high
615   pressure and high temperature and the internal structure of Mars. Science, 268, 1892–
616   1894. https://doi.org/10.1126/science.268.5219.1892

617 Fei, Y., Bertka, C.M. and Finger, L.W., 1997. High-pressure iron-sulfur compound, Fe_3S_2, and
618   melting relations in the Fe–FeS system. Science, 275, 1621–1623.
619   https://doi.org/10.1126/science.275.5306.1621

620 Fei, Y., Li, J., Bertka, C.M. and Prewitt, C.T., 2000. Structure type and bulk modulus of Fe_3S, a
621   new iron-sulfur compound. Am. Mineral., 85, 1830–1833.
622   https://doi.org/10.2138/am-2000-11-1229

623 Fei, Y., Ricolleau, A., Frank, M., Mibe, K., Shen, G. and Prakapenka, V., 2007. Toward an
624   internally consistent pressure scale. Proc. Natl. Acad. Sci. U.S.A., 104, 9182–9186.
625   https://doi.org/10.1073/pnas.0609013104

626 Frank, K. and Schubert, K., 1971. Kristallstruktur von $Ni_{31}Si_{12}$. Acta crystallogr., B Struct.

crystallogr. cryst. chem., 27, 916–920. https://doi.org/10.1107/S0567740871003261

Heinz, D.L., and Jeanloz, R., 1987. Measurement of the melting curve of $Mg_{0.9}Fe_{0.1}SiO_3$ at lower mantle conditions and its geophysical implications. J. Geophys. Res., 92, 437–444. https://doi.org/10.1029/JB092iB11p11437

Irving, J.C., Cottaar, S. and Lekić, V., 2018. Seismically determined elastic parameters for Earth's outer core. Sci. Adv., 4, 2538. https://doi.org/10.1126/sciadv.aar2538

Jephcoat, A. and Olson, P., 1987. Is the inner core of the Earth pure iron? Nature, 325, 332–335. https://doi.org/10.1038/325332a0

Jones, J.H. and Drake, M.J., 1983. Experimental investigations of trace element fractionation in iron meteorites, II: The influence of sulfur. Geochim. Cosmochim. Acta., 47, 1199–1209. https://doi.org/10.1016/0016-7037(83)90062-5

Kamada, S., Terasaki, H., Ohtani, E., Sakai, T., Kikegawa, T., Ohishi, Y., Hirao, N., Sata, N. and Kondo, T., 2010. Phase relationships of the Fe–FeS system in conditions up to the Earth's outer core. Earth Planet. Sci. Lett., 294, 94–100. https://doi.org/10.1016/j.epsl.2010.03.011

Kamada, S., Ohtani, E., Terasaki, H., Sakai, T., Miyahara, M., Ohishi, Y. and Hirao, N., 2012. Melting relationships in the Fe–Fe_3S system up to the outer core conditions. Earth Planet. Sci. Lett., 359, 26–33. https://doi.org/10.1016/j.epsl.2012.09.038

Kamada, S., Ohtani, E., Terasaki, H., Sakai, T., Takahashi, S., Hirao, N. and Ohishi, Y., 2014. Equation of state of Fe_3S at room temperature up to 2 megabars. Phys. Earth Planet. Inter., 228, 106-113. https://doi.org/10.1016/j.pepi.2013.11.001

Kantor, I., Prakapenka, V., Kantor, A., Dera, P., Kurnosov, A., Sinogeikin, S., Dubrovinskaia, N. and Dubrovinsky, L., 2012. BX90: A new diamond anvil cell design for X-ray diffraction and optical measurements. Rev. Sci. Instrum., 83, 125102. https://doi.org/10.1063/1.4768541

King, H. and Prewitt, C.T., 1982. High-pressure and high-temperature polymorphism of iron sulfide (FeS). Acta crystallogr., B Struct. crystallogr. cryst. chem., 8, 1877–1887. https://doi.org/10.1107/S0567740882007523

Kjekshus, A., Skaug, K.E., Hebrew, C., Van Buren, C.T., Klæboe, P. and Swahn, C.G., 1973. On the crystal structure of Ni_5As_2. Acta Chem. Scand., 27, 582–588.

Kruijer, T.S., Touboul, M., Fischer-Gödde, M., Bermingham, K.R., Walker, R.J. and Kleine, T., 2014. Protracted core formation and rapid accretion of protoplanets. Science, 344, 1150–1154. https://doi.org/10.1126/science.1251766

Kuwayama, Y., Morard, G., Nakajima, Y., Hirose, K., Baron, A.Q., Kawaguchi, S.I., Tsuchiya, T., Ishikawa, D., Hirao, N. and Ohishi, Y., 2020. Equation of state of liquid iron under extreme conditions. Phys. Rev., 124, .165701. https://doi.org/10.1103/PhysRevLett.124.165701

Litasov, K.D., Shatskiy, A.F., Minin, D.A., Kuper, K.E. and Ohfuji, H., 2019. The Ni–Ni_2P phase diagram at 6 GPa with implication to meteorites and super-reduced terrestrial rocks. High Press. Res., 39, 561–578. https://doi.org/10.1080/08957959.2019.1672677

Maaref, S., Madar, R., Chaudouet, P., Fruchart, R., Senateur, J.P., Averbuch-Pouchot, M.T.,

Bacmann, M., Durif, A. and Wolfers, P., 1983. Etude de la structure et des conditions de stabilite d'un nouvel arseniure de fer: $Fe_{12}As_5$. Mater. Res. Bull., 18, 473-480. https://doi.org/10.1016/0025-5408(83)90139-3

Malvin, D.J., Wang, D. and Wasson, J.T., 1984. Chemical classification of iron meteorites—X. Multielement studies of 43 irons, resolution of group IIIE from IIIAB, and evaluation of Cu as a taxonomic parameter. Geochim. Cosmochim. Acta., 48, 785–804. https://doi.org/10.1016/0016-7037(84)90101-7

Masters, G. and Gubbins, D., 2003. On the resolution of density within the Earth. Phys. Earth Planet. Inter., 140, 159–167. https://doi.org/10.1016/j.pepi.2003.07.008

McDonough, W.F. and Sun, S.S., 1995. The composition of the Earth. Chem. Geol., 120, 223–253. https://doi.org/10.1016/0009-2541(94)00140-4

McDonough, W.F., 2003. Compositional model for the Earth's core. In The Mantle and Core (Ed. R. W. Carlson), Vol. 2 Treatise on Geochemistry (Exec. Eds. H. D. Holland and K. K. Turekian), 547–568.

Momma, K. and Izumi, F., 2011. VESTA 3 for three-dimensional visualization of crystal, volumetric and morphology data. J. Appl. Crystallogr., 44, 1272–1276. https://doi.org/10.1107/S0021889811038970

Morard, G., Andrault, D., Guignot, N., Sanloup, C., Mezouar, M., Petitgirard, S. and Fiquet, G., 2008. In situ determination of $Fe–Fe_3S$ phase diagram and liquid structural properties up to 65 GPa. Earth Planet. Sci. Lett., 620–626. https://doi.org/10.1016/j.epsl.2008.05.028

Mori, Y., Ozawa, H., Hirose, K., Sinmyo, R., Tateno, S., Morard, G. and Ohishi, Y., 2017. Melting experiments on $Fe–Fe_3S$ system to 254 GPa. Earth Planet. Sci. Lett., 464 135–141. https://doi.org/10.1016/j.epsl.2017.02.021

Murthy, V.R. and Hall, H.T., 1970. The chemical composition of the earth's core: Possibility of sulfur in the core. Phys. Earth Planet. Inter., 2, 276–282. https://doi.org/10.1016/0031-9201(70)90014-2

Nimmo, F., 2015. Thermal and compositional evolution of the core. In Core Dynamics (Ed. Peter Olsen). Vol. 8 Treatise on Geophysics, (Exec. Eds. G. Schubert), 217–241.

Okada, A., Kobayashi, K., Ito, T. and Sakurai, T., 1991. Structure of synthetic perryite, $(Ni, Fe)_8(Si, P)_3$. Acta Crystallogr. C Struct. Chem., 47, 1358–1361. https://doi.org/10.1107/S0108270191000483

Oryshchyn, S., Babizhetskyy, V., Zhak, O., Stoyko, S., Guérin, R., and Simon, A., 2011. Crystal structure of $HT-Ni_5P_2$ and reinvestigation of isotypic Ni_5As_2. Intermetallics, 19, 1041–1046. https://doi.org/10.1016/j.intermet.2011.03.013

Ozawa, H., Hirose, K., Suzuki, T., Ohishi, Y. and Hirao, N., 2013. Decomposition of Fe_3S above 250 GPa. Geophys. Res. Lett., 40, 4845–4849. https://doi.org/10.1002/grl.50946

Prakapenka, V.B., Kubo, A., Kuznetsov, A.Laskin, A., Shkurikhin, O., Dera, P., Rivers, M. L. and Sutton, S.R., 2008. Advanced flat top laser heating system for high pressure research at GSECARS: application to the melting behavior of germanium. High Press. Res., 28, 225–235. https://doi.org/10.1080/08957950802050718

Prescher, C., and Prakapenka, V.B., 2015. DIOPTAS: a program for reduction of two
        dimensional X-ray diffraction and data exploration. High Press. Res., 35(3), 223– 230.
        https://doi.org/10.1080/08957959.2015.1059835

Ricard, Y., Šrámek, O. and Dubuffet, F., 2009. A multi-phase model of runaway core–mantle
        segregation in planetary embryos. Earth Planet. Sci. Lett., 284, 144–150.
        https://doi.org/10.1016/j.epsl.2009.04.021

Rigaku Oxford Diffraction, 2018. CrysAlisPRO software system, ver. 1.171.39.44a Rigaku
        Corporation, Oxford, U.K.

Ringwood, A.E., 1966. The chemical composition and origin of the Earth. Advances in earth
        science, 65, 287.

Rubie, D.C., Frost, D.J., Mann, U., Asahara, Y., Nimmo, F., Tsuno, K., Kegler, P., Holzheid, A.
        and Palme, H., 2011. Heterogeneous accretion, composition and core–mantle
        differentiation of the Earth. Earth Planet. Sci. Lett., 301, 31–42.
        https://doi.org/10.1016/j.epsl.2010.11.030

Rundqvist, S., 1960. The structures of Co_2P, Ru_2P and related phases. Acta Chem.
        Scand., 14, 1961–1979.

Rundqvist, S. and Jellinek, F., 1959. The structures of Ni_6Si_2B, Fe_2P and some related phases.
        Acta Chem. Scand., 13, 425–432.

Saini, G.S., Calvert, L.D., and Taylor, J.B., 1964. Compounds of the type M_5X_2: Pd_5As_2, Ni_5Si_2,
        and Ni_5P_2. Can. J. Chem., 42, 1511–1517. https://doi.org/10.1139/v64-233

Scott, E.R. and Wasson, J.T., 1975. Classification and properties of iron meteorites. Rev.
        Geophys., 13, 527–546. https://doi.org/10.1029/RG013i004p00527

Seagle, C.T., Campbell, A.J., Heinz, D.L., Shen, G. and Prakapenka, V.B., 2006. Thermal
        equation of state of Fe_3S and implications for sulfur in Earth's core. J. Geophys. Res. Solid
        Earth, 111. https://doi.org/10.1029/2005JB004091

Shannon, M.C. and Agee, C.B., 1996. High pressure constraints on percolative core formation.
        Geophys. Res. Lett., 23, 2717–2720. https://doi.org/10.1029/96GL02817

Sheldrick, G.M., 2015. Crystal structure refinement with SHELXL. Acta Crystallogr. C Struct.
        Chem., 71, 3–8. https://doi.org/10.1107/S2053229614024218

Stevenson, D.J., 1981. Models of the Earth's core. Science, 214, 611–619.
        https://doi.org/10.1126/science.214.4521.611

Stevenson, D.J., 1988. Fluid dynamics of core formation. In Topical Conference Origin of the
        Earth (Vol. 681, p. 87).

Tateno, S., Ozawa, H., Hirose, K., Suzuki, T., I-Kawaguchi, S., and Hirao, N., 2019. Fe_2S: the
        most Fe-rich iron sulfide at the Earth's inner core pressures. Geophys. Res. Lett., 46,
        11,944–11,949. https://doi.org/10.1029/2019GL085248

Wasson, J.T. and Wai, C.M., 1970. Composition of the metal, schreibersite and perryite of
        enstatite achondrites and the origin of enstatite chondrites and achondrites. Geochim.
        Cosmochim. Acta, *34*, 169-184. https://doi.org/10.1016/0016-7037(70)90004-9

Yoshino, T., Walter, M.J. and Katsura, T., 2003. Core formation in planetesimals triggered by

748   permeable flow. Nature, 422, 154–157. https://doi.org/10.1038/nature01459

749 Yokoo, S., Hirose, K., Sinmyo, R. and Tagawa, S., 2019. Melting experiments on liquidus phase
750   relations in the Fe-S-O ternary system under core pressures. Geophys. Rev. Lett., 46,
751   5137–5145. https://doi.org/10.1029/2019GL082277

752 Zurkowski, C.C., Lavina, B., Chariton, S., Tkachev, S., Prakapenka V.B. and Campbell A.J.,
753   *in press*. The crystal structure of Fe_2S at 90 GPa based on single-crystal X-ray diffraction
754   techniques. American Mineralogist, https://doi.org/10.2138/am-2022-7973

755 Zurkowski, C. C., Lavina, B., Brauser, N. M., Davis, A. H., Chariton, S., Tkachev, S.,
756   Greenberg, E., Prakapenka, V. B., and Campbell, A. J., *in press.* Pressure-induced *C*23-
757   *C*37 transition and compression behavior of orthorhombic Fe_2S to Earth's core pressures
758   and high temperatures. https://doi.org/10.2138/am-2022-8187

759